Central Lancashire Online Knowledge (CLoK)

Title	Revised optical classification of a sample of gamma-ray emitting AGN with GTC and VLT
Type	Article
URL	https://knowledge.lancashire.ac.uk/id/eprint/57557/
DOI	https://doi.org/10.1051/0004-6361/202557187
Date	2026
Citation	Dalla Barba, B., Foschini, L., Berton, M., Järvelä, E., Marziani, P., Ciroi, S., Dalla Bontà, Elena, Crepaldi, L., Vietri, A. et al (2026) Revised optical classification of a sample of gamma-ray emitting AGN with GTC and VLT. Astronomy & Astrophysics, 705. A122. ISSN 0004-6361
Creators	Dalla Barba, B., Foschini, L., Berton, M., Järvelä, E., Marziani, P., Ciroi, S., Dalla Bontà, Elena, Crepaldi, L., Vietri, A., Antón, S., Marchã, M. J. M., Condò, P. and Mazzucchelli, C.

Astronomy & Astrophysics

Revised optical classification of a sample of gamma-ray-emitting active galactic nuclei with GTC and VLT

B. Dalla Barba[1,2,★], L. Foschini[2], M. Berton[3], E. Järvelä[4], P. Marziani[5], S. Ciroi[6], E. Dalla Bontá[6,5,7], L. Crepaldi[6,8], A. Vietri[5,6], S. Antón[9], M. J. M. Marchã[10], P. Condó[11], and C. Mazzucchelli[12]

[1] Universitá degli studi dell'Insubria, Via Valleggio 11, Como 22100, Italy
[2] Osservatorio Astronomico di Brera, Istituto Nazionale di Astrofisica (INAF), Via E. Bianchi 46, Merate (LC) 23807, Italy
[3] European Southern Observatory (ESO), Alonso de Córdova 3107, Vitacura Santiago, Chile
[4] Department of Physics and Astronomy, Texas Tech University, Box 41051, Lubbock 79409-1051, TX, USA
[5] Osservatorio Astronomico di Padova, Istituto Nazionale di Astrofisica (INAF), Vicolo dell'Osservatorio 5, 35122 Padova, Italy
[6] Dipartimento di Fisica e Astronomia "G. Galilei", Università degli studi di Padova, Vicolo dell'Osservatorio 3, Padova 35122, Italy
[7] Jeremiah Horrocks Institute, University of Central Lancashire, Preston PR1 2HE, UK
[8] Osservatorio Astronomico di Cagliari, Istituto Nazionale di Astrofisica (INAF), Via della Scienza 5, 09047 Selargius, Italy
[9] CFisUC, Departamento de Física, Universidade de Coimbra, 3004-516 Coimbra, Portugal
[10] Dept. of Physics & Astronomy and Dept. of Computer Science, University College London, Gower Street, London WC1E 6BT, UK
[11] Dipartimento di Fisica, Università di Roma Tor Vergata, Via della Ricerca Scientifica 1, 00133 Roma, Italy
[12] Instituto de Estudios Astrofísicos, Facultad de Ingeniería y Ciencias, Universidad Diego Portales, Avenida Ejercito Libertador 441, Santiago, Chile

ABSTRACT

We report the results of the optical follow-up of a sample of γ-ray-emitting active galactic nuclei (AGNs). New high-quality optical spectra were obtained using the Gran Telescopio Canarias with the Optical System for Imaging and low-Intermediate-Resolution Integrated Spectroscopy and the European Southern Observatory's Very Large Telescope Unit Telescope 1 with the FOcal Reducer and low dispersion Spectrograph 2. From the analysis of these spectra, we confirmed the previous narrow-line Seyfert 1 (NLS1) classification for four objects and discovered two new NLS1s, bringing the total number of optically confirmed γ-NLS1s to 26. We also identified two ambiguous cases between NLS1 and intermediate Seyfert (IS), three ISs, one broad-line Seyfert 1, and one Seyfert 2. Based on the new spectra, we calculated black hole masses ranging from $10^{6.25}$ to $10^{9.32}$ M$_\odot$ and Eddington ratios spanning 0.05 to 2.07. This reclassification provides support for the scenario in which AGNs with relatively low black hole masses are capable of launching powerful relativistic jets and contributes to our broader understanding of γ-ray-emitting AGNs.

Key words. galaxies: active – galaxies: jets – quasars: emission lines – galaxies: Seyfert

1. Introduction

The active galactic nuclei (AGNs) family is proving to be increasingly complex and diverse. A classical distinction exists between jetted and non-jetted AGNs (Padovani et al. 2017). We can further divide the jetted class into three main categories: flat-spectrum radio quasars (FSRQs), BL Lacertae objects (BL Lacs), and jetted narrow-line Seyfert 1s (NLS1s), together with their misaligned counterparts. Misaligned AGNs are characterized by large viewing angles, while the jet axes of FSRQs, BL Lacs, and NLS1s are directed toward the Earth (for recent reviews, see, e.g., Foschini 2017 and Blandford et al. 2019).

The optical spectra of jetted AGNs display a wide range of features, from prominent emission lines – as in the case of FSRQs and γ-ray NLS1s – to weak or absent lines, as observed in BL Lacs. The same applies to misaligned AGNs. Of particular interest is the distinction between FSRQs and γ-ray NLS1s. Both can exhibit Balmer and forbidden lines, but NLS1s are classically defined by the presence of weak oxygen lines ([O III]/Hβ < 3) and strong iron emission. The main discriminant between NLS1s and FSRQs lies in the full width at half maximum (FWHM) of the Hβ line: above 2000 km s^{-1} for FSRQs and below 2000 km s^{-1} for NLS1s (Osterbrock & Pogge 1985; Goodrich 1989).

After the discovery of γ-NLS1s, many open questions arose or gained new relevance, such as what the role of γ-NLS1s in the blazar sequence is given their low black hole masses, and whether γ-NLS1s can help pinpoint the region where γ-rays are produced in AGNs. The answer to the first question came in 2016, when Berton et al. (2016) suggested that γ-ray NLS1s represent the low-mass and low-luminosity tail of the blazar distribution. The answer to the second question is more complex, and different studies have presented contrasting results. Some support a central origin for the γ-rays (in the broad-line region or dusty torus; see, e.g., Marscher et al. 2008; Ghisellini et al. 2014), while others favor a more distant origin (in the narrow-line region; see, e.g., Foschini et al. 2019; Dalla Barba et al. 2025). In both cases, γ-NLS1s serve as a unique laboratory for investigating the AGN jet phenomenon.

Our knowledge of the impact of NLS1s on the population of γ-ray sources is currently limited by the small number of

known objects of this type. To address this, Foschini et al. (2022) selected a sample of 2980 optically identified γ-ray-emitting sources from the fourth *Fermi* Gamma-ray Large Area Telescope (*Fermi*-LAT) catalog (4FGL) and searched for available optical spectra in the literature. This led to a reclassification of a significant portion of the sample. However, many of the public observations were carried out in the 1970s-1980s and suffer from low spectral resolution and/or poor quality, which prevented a reliable classification. For these ambiguous (AMB) cases and for the candidate NLS1 found by Foschini et al. (2022), we obtained new optical spectra for a total of 22 objects, 6 in the Northern Hemisphere and 17 in the Southern Hemisphere. We excluded a few cases (see below) for a final sample of 18 objects (see Table 1). These spectra allowed us to search for additional cases of γ-NLS1s and to increase the number of known sources in this family.

At the same time, we identified some cases of intermediate Seyferts (ISs), a subclass of Seyfert galaxies characterized by a peculiar spectral shape of the permitted lines (Osterbrock & Koski 1976). Owing to the intermediate viewing angle, the observer can detect radiation from both narrow-line regions (NLRs) and broad-line regions (BLRs), resulting in a composite line profile with broad wings and a narrow core. These two contributions are usually modeled with separate Gaussian components, referred to as the broad and narrow components, whose combination reproduces the total observed emission. Because of the peculiar spectral shape of Hβ, ISs are often misclassified as NLS1s, and vice versa (see, e.g., Järvelä et al. 2020; Crepaldi et al. 2025). Disentangling the two classes requires high-resolution spectra, as confirmed by the borderline NLS1-IS cases found in our sample. Moreover, according to the unified model (Keel 1980; Antonucci 1993; Urry & Padovani 1995), the intermediate viewing angle expected for ISs makes their γ-ray detection particularly puzzling with respect to jet orientation. The inclusion of NLS1s and ISs as γ-ray-emitting AGNs will help us investigate the jetted AGN phenomenon in greater detail, including classes of sources that are often overlooked.

The structure of this paper is as follows. In Sect. 2 we describe the observations and the data analysis. In Sect. 3 we list the classification criteria. In Sect. 4 we explain how we estimated the physical parameters, including the black hole mass (M_{BH}) and the Eddington ratio (R_{Edd}). In Sect. 5 we provide details of the individual analyzed objects. In Sect. 6 we discuss the new classifications and present our conclusions. Throughout this paper, we adopt a standard Λ Cold Dark Matter cosmology with $H_0 = 73.3 \, \mathrm{km \, s^{-1} \, Mpc^{-1}}$, $\Omega_{matter} = 0.3$, and $\Omega_{vacuum} = 0.7$ (Riess et al. 2022).

2. Observations and data analysis

From the original sample of nearly 3000 objects analyzed by Foschini et al. (2022), we selected a subsample of 22 sources for which we requested high-quality spectra. The subsample is the result of the selection of those objects classified by Foschini et al. (2022) as NLS1 or AMB in their paper, taking also into account for the observability of the objects. The objects are divided into two groups: those in the Northern Hemisphere and those in the Southern Hemisphere.

The new data were collected using the Optical System for Imaging and low-Intermediate-Resolution Integrated Spectroscopy (OSIRIS), mounted on the Gran Telescopio Canarias (GTC) in the Northern Hemisphere (Program GTC33-22B, PI: E. Järvelä), and the FOcal Reducer/low dispersion Spectro-

graph 2 (FORS2), mounted on Unit Telescope 1 of the Very Large Telescope (UT1/VLT) in the Southern Hemisphere (Programs 110.23UC.003, PI: C. Mazzucchelli; 111.24P0.002, PI: M. Berton). The OSIRIS sample comprises 6 sources. The FORS2 sample initially included 17 objects as part of a filler program designed for observations during nonoptimal conditions at Paranal. The UT1 observations cover 12 of the 17 objects; one spectrum corresponds to PKS 2004−447 (J2007−4432), which was excluded from this analysis as it has already been studied in detail by Berton et al. (2021), and the other four spectra show only forbidden narrow lines with FWHM dominated by instrumental broadening. As such, they cannot be used to refine the classification or to derive reliable physical parameters. The final sample, consisting of 18 objects, is listed in Table 1.

The GTC observations were carried out with the following setup: a 1″ slit and the R1000R grism, yielding a spectral resolution of $R = \lambda/\Delta\lambda = 1122$[1]. Standard stars were observed with a 2.52″ slit. The OSIRIS spectral coverage is 3650–10 000 Å. The UT1/VLT setup was: a 1″ slit and the 300V grism, resulting in a spectral resolution of $R = 440$[2]. The FORS2 spectral coverage is 3300–11 000 Å. Further details are provided in Table 1.

The reduction of the GTC data was carried out with a standard procedure using IRAF (version 2.18; Tody 1986, 1993). For VLT observations, we used the already reduced data that can be found in the European Southern Observatory (ESO) archive[3].

Due to the different slit apertures used for the sources and the standard stars in the GTC observations, a flux correction was applied to the final spectra. Next, for each spectrum, we corrected for reddening and identified the main optical emission lines to compute the redshift (z). The redshift was calculated as the flux-weighted average of the individual z values derived from the [O II]λ3727, Hβ, and [O III]$\lambda\lambda$4959,5007 lines, when present. In one case, J2354−0958, the measured redshift differed significantly from the value reported in the literature; see Sect. 5.18 for details. The resulting redshifts are listed in Table A.1. Continuum subtraction was performed using the dedicated IRAF function. Iron multiplets emission lines were removed using the tool developed by Kovačević et al. (2010) and Shapovalova et al. (2012), available through the Serbian Virtual Observatory[4]. The iron fitting allows us to calculate the R_{4570} parameter, defined as the ratio between the flux of the blueward iron bump (relative to Hβ) and the flux of the Hβ line.

After these preprocessing steps, we fitted the Hβ–[O III] complex, where feasible. In some spectra, the region around Hβ and [O III] was too noisy (e.g., J0102+4214), or significantly affected by atmospheric absorption (e.g., J0224+0700). In such cases, we fitted only the [O III]$\lambda\lambda$4959,5007 lines, or alternatively the Mg II λ2800 line. We did not perform a telluric correction because the resulting spectral profile cannot be completely trusted to calculate the FWHM and to propose a reliable classification of the AGN.

The Hβ line was modeled using four alternative profiles: three Gaussians, two Gaussians, one Gaussian, or a Lorentzian. The first two profiles are typically attributed to IS, when the broad and the narrow component are clearly separable, but they can also fit NLS1 well in low- or intermediate-resolution spectra (Dalla Barba et al. 2023). The single Gaussian with a

---

[1] https://www.gtc.iac.es/instruments/osiris+/osiris+.php#Longslit_Spectroscopy
[2] https://www.eso.org/sci/facilities/paranal/instruments/fors/overview.html
[3] https://archive.eso.org/scienceportal/home
[4] http://servo.aob.rs/FeII_AGN/

FWHM comparable to the one of narrow lines is typical of type 2 AGNs. The Lorentzian profile, instead, is typical of NLS1 (Sulentic et al. 2002, 2009; Goad et al. 2012; Cracco et al. 2016; Berton et al. 2020).

For the [O III]$\lambda\lambda$4959,5007 doublet, a single Gaussian was sufficient in most cases; however, a two-Gaussian model was adopted when required. This composite model includes a narrow core component from the NLR and an additional outflow component. The two [O III] lines were tied in terms of FWHM, central wavelength, and flux, assuming the theoretical intensity ratio of 2.993 ± 0.014 (Dimitrijević et al. 2007). Parameter uncertainties were estimated using a Monte Carlo method creating $N = 1000$ synthetic spectra. For each iteration, we added a Gaussian noise to the line profile, proportional to the standard deviation of the signal in the continuum between 5050 and 5150 Å.

3. Classification criteria

As already introduced in Sect. 1, the optical classification of jetted AGNs is not always straightforward, especially when dealing with low-S/N spectra. This is particularly true for ISs and NLS1s, which are often prone to misclassification. The difficulty mainly arises from the similarity in the observed Hβ line profiles when its FWHM is close to $2000\,\mathrm{km\,s^{-1}}$, the conventional threshold adopted to distinguish NLS1s from broader-lined sources (see, e.g., Fig. 2 in Dalla Barba et al. 2023).

Indeed, a Lorentzian profile – commonly used to model the permitted lines in NLS1s – can resemble a composite of two or more Gaussian components, typically employed for ISs (and vice versa). This degeneracy in fitting can lead to AMB classifications, particularly in low-resolution or noisy spectra. From a physical standpoint, the Lorentzian shape is generally associated with turbulent motions in the BLR, while the Gaussian components are interpreted as arising from clouds in Keplerian motion within the BLR (e.g., Kollatschny & Zetzl 2011; Goad et al. 2012). This highlights that the choice of model to fit the Hβ line is not merely a technical matter but reflects underlying physical conditions. Therefore, the distinction between ISs and NLS1s is not only observational but also tied to the kinematics and structure of the BLR, and cannot be attributed solely to orientation effects.

Furthermore, the Hβ line profile can exhibit marked asymmetries. Such asymmetries can arise from a variety of physical processes. One possibility is the presence of an outflow, often modeled as a moving bubble of ionized gas, which can produce blue- or red-asymmetric line wings (e.g., Boroson & Green 1992). Another potential explanation involves double-peaked emission lines, which can originate from a rotating Keplerian disk around the central black hole (e.g., Dumont & Collin-Souffrin 1990; Chen et al. 1989). Finally, asymmetric and systematically shifted line profiles have been proposed as possible signatures of close binary supermassive black holes, where the orbital motion of the BLRs around the two black holes induces observable Doppler shifts (e.g., Gaskell 1996). While these more complex scenarios are fascinating, they typically manifest in distinctly double-peaked broad-line profiles, which are not observed in the present sample. Therefore, such interpretations can be reasonably excluded in the context of this work. Nonetheless, the variety of possible Hβ profiles illustrates the necessity for careful spectral modeling and a multifaceted classification approach when dealing with jetted AGNs.

These considerations underscore the intrinsic challenges in providing a conclusive optical classification for AGNs, particularly when relying solely on spectral features that can be affected by noise, resolution, and modeling degeneracies. Despite these limitations, in the following we outline the empirical criteria adopted to classify the objects in the present sample. These criteria aim to balance the need for physical consistency with the constraints imposed by the available data:

- NLS1s: Sources showing a Lorentzian Hβ profile or a multiple-Gaussian fit with smooth wings (i.e., no distinct separation between the NLR and the BLR), with a total FWHM $< 2000\,\mathrm{km\,s^{-1}}$. These spectra typically exhibit weak [O III] lines, with [O III]/Hβ < 3, and often show the presence of optical Fe II multiplets.

- Broad-line Seyfert 1s (BLS1s): Classical type 1 AGNs characterized by a broad Hβ line with a total FWHM $> 2000\,\mathrm{km\,s^{-1}}$. The H$\beta$ profile can be fit by either a single Gaussian or multiple components, but the broadness is the defining feature.

- ISs: AGNs that show multiple-Gaussian Hβ profiles with a clear separation between the NLR and BLR components. Unlike NLS1s, no strict cut is imposed on the [O III]/Hβ flux ratio or on the presence of Fe II lines. This class includes Seyfert 1.2–1.9 types and generally exhibits intermediate obscuration between type 1 and type 2 AGNs.

- Seyfert 2s (SY2s): Sources displaying only narrow emission lines, typically with FWHMs of $\sim1000\,\mathrm{km\,s^{-1}}$. They are associated with type 2 AGNs and are interpreted as systems viewed edge on such that the BLR is obscured or totally absent (see the case of true SY2, e.g. Pogge 2003; Bianchi et al. 2012; Miniutti et al. 2013 and references therein).

- AMBs: A heterogeneous class reported by Foschini et al. (2022), including objects for which no reliable classification could be assigned. These cases lack crucial information such as published optical spectra, measurable Hβ FWHM, or reliable positional cross-identification. Furthermore, the viewing angle remains unconstrained.

4. Physical parameters

4.1. Black hole mass (M_{BH})

To estimate the black hole mass, we adopted Eqs. (38) and (40) from Dalla Bontà et al. (2020), which relates M_{BH} to the luminosity and line width of Hβ – specifically, the second-order moment ($\sigma_{\mathrm{H}\beta}$) or the FWHM in the case of Lorentzian profiles. As noted by Dalla Bontà et al. (2020), the second-order moment is generally preferred over the FWHM as it yields tighter correlations with black hole mass. Furthermore, these relations avoid the intermediate step involving the continuum luminosity at 5100 Å, which is a significant advantage when analyzing jetted sources. In such cases, jet emission can contaminate the continuum, leading to an overestimation of the black hole mass.

The adopted equations are

$$\log\left(\frac{M_{\mathrm{BH}}}{M_\odot}\right) = \log(f) + 7.530 + 0.703 \times \left[\log\left(\frac{L_{\mathrm{H}\beta_{\mathrm{broad}}}}{\mathrm{erg\,s^{-1}}}\right) - 42\right] +$$
$$+ 2.183 \times \left[\log\left(\frac{\sigma_{\mathrm{H}\beta}}{\mathrm{km\,s^{-1}}}\right) - 3.5\right] \quad (1)$$

$$\log\left(\frac{M_{\mathrm{BH}}}{M_\odot}\right) = \log(f) + 7.015 + 0.784 \times \left[\log\left(\frac{L_{\mathrm{H}\beta_{\mathrm{broad}}}}{\mathrm{erg\,s^{-1}}}\right) - 42\right] +$$
$$+ 1.387 \times \left[\log\left(\frac{\mathrm{FWHM(H}\beta)}{\mathrm{km\,s^{-1}}}\right) - 3.5\right], \quad (2)$$

Table 1. Sources and their observation details.

Name	Alias	RA (J2000) [h:m:s]	Dec (J2000) [°:′:″]	z_{pub}	Tel.	Obs. Date [yyyy-mm-dd]	Exp. time [s]	Airmass	Seeing [″]
J0102+4214	GB6 J0102+4214	01:02:27.1	+42:14:18.9	0.874	GTC	2022-09-04	600	1.35	–
J0224+0700	PKS 0221+067	02:24:28.4	+06:59:23.3	0.511	GTC	2022-09-04	600	1.08	–
J0422−0644	PMN J0422−0643	04:22:10.8	−06:43:45.3	0.242	UT1	2023-01-25	1800	1.88	0.71
J0442−0017	PKS 0440−00	04:42:38.7	−00:17:43.4	0.844	UT1	2023-07-19	1830	1.94	0.53
J0515−4556	PKS 0514−459	05:15:45.3	−45:56:43.2	0.194	UT1	2022-11-25	1800	1.13	0.85
J0521−1734	TXS 0519−176	05:21:23.6	−17:37:30.1	0.347	UT1	2022-12-03	1800	1.07	1.65
J0932+5306	S4 0929+53	09:32:41.2	+53:06:33.8	0.597	GTC	2022-10-30	300	1.30	–
J1048−1912	PKS 1045−18	10:48:06.6	−19:09:35.7	0.595	UT1	2022-12-17	1800	1.10	2.08
J1102+5251	GB6 J1102+5249	11:02:49.8	+52:50:12.7	0.690	GTC	2022-11-16	600	1.26	–
J1154+4037	B3 1151+408	11:53:54.7	+40:36:52.6	0.923	GTC	2022-11-24	600	1.35	–
J1202−0528	PKS 1200−051	12:02:34.2	−05:28:02.5	0.381	UT1	2023-01-20	1800	1.17	0.55
J1246−2548	PKS 1244−255	12:46:46.8	−25:47:49.3	0.638	UT1	2023-07-10	1830	1.64	1.77
J1310+5514	TXS 1308+554	13:11:03.2	+55:13:54.3	0.926	GTC	2022-11-28	900	1.57	–
J1331−1325	PMN J1331−1326	13:31:20.4	−13:26:05.6	0.250	UT1	2023-07-15	1830	1.26	0.66
J1818+0903	NVSS J181840+090346	18:18:40.1	+09:03:46.2	0.354	UT1	2023-06-22	1830	1.20	0.58
J1902−6748	PMN J1903−6749	19:03:01.2	−67:49:35.9	0.255	UT1	2023-06-19	1830	1.37	1.24
J2325−3559	CTS 0490	23:25:28.6	−35:57:54.2	0.360	UT1	2023-07-19	1830	1.04	1.72
J2354−0958	PMN J2354−0957	23:54:05.5	−09:57:48.8	0.272	UT1	2023-06-28	1830	1.47	1.08

Notes. The seeing parameter is the average of the values recorded at the beginning and at the end of the observation. It is reported only for the UT1/VLT observations, as it is not available in the headers of the GTC data.

where $\sigma_{H\beta}$ is the second-order moment. The relations show a scatter of 0.309 dex and 0.371 dex, respectively. The geometrical factor adopted is the total value reported by Collin et al. (2006), in order to avoid assumptions about the population nature of our sample. It corresponds to $f = (3.85 \pm 1.15)$. $L_{H\beta_{broad}}$ denotes the luminosity of the broad component of the Hβ line.

For sources in which the Hβ line is not detected – due to either absorption or spectral noise – we estimated the black hole mass using the Mg IIλ2800 or [O III]λ5007 lines. Relations based on Mg IIλ2800 suffer from the same issue as Hβ when the continuum contribution at 3000 Å is included. For this reason, we adopted the relation from Trakhtenbrot & Netzer (2012):

$$\log\left(\frac{M_{BH}}{M_{\odot}}\right) = 6.83 + 0.5 \times \log\left(\frac{L_{Mg\,II}}{10^{42}\ erg\ s^{-1}}\right)$$
$$+ 2 \times \log\left[\frac{FWHM(Mg\,II)}{10^3\ km\ s^{-1}}\right], \quad (3)$$

which relies solely on the luminosity and FWHM of the Mg IIλ2800 line, thus avoiding the use of the continuum luminosity. The scattering for this relation is of 0.13 dex.

The relations based on [O III], however, are known to provide less reliable results, and we therefore treated the corresponding mass estimates as upper limits. The tendency of [O III] to overestimate black hole masses in active galaxies has already been discussed by Ho & Kim (2014). For these cases, we used the revised $M - \sigma_{\star}$ relation from Ho & Kim (2014):

$$\log\left(\frac{M_{BH}}{M_{\odot}}\right) = 8.49^{+0.052}_{-0.107} + (4.38 \pm 0.29) \times \log\left(\frac{\sigma_{\star}}{200\ km\ s^{-1}}\right), \quad (4)$$

where $\sigma_{\star} = FWHM([O\,III]_{core})/2.35$, and FWHM([O III]$_{core}$) is the width of the core component only. The limitation of this method is evident in Fig. 4 of Greene & Ho (2005), where the data show a significant scatter around the relation. The results for all sources are reported in Table A.1.

4.2. Eddington ratio (R_{Edd})

The Eddington ratio is calculated as

$$R_{Edd} = \frac{L_{bol}}{L_{Edd}} = \frac{L_{bol}}{1.3 \times 10^{38}\,(M_{BH}/M_{\odot})}. \quad (5)$$

The black hole mass used is the one derived in the previous paragraph. The bolometric luminosity (L_{bol}), on the other hand, can be estimated using the classical relation $L_{bol} = 9 \times \lambda L_{\lambda}(5100\ \text{Å})$ from Kaspi et al. (2000), or with a revised version from Netzer (2019):

$$L_{bol} = k_{bol} \times \lambda L_{\lambda}(5100\ \text{Å}) \quad ; \quad k_{bol} = 40 \cdot \left[\frac{\lambda L_{\lambda}(5100\ \text{Å})}{10^{42}\ erg\ s^{-1}}\right]^{-0.2}, \quad (6)$$

where $\lambda L_{\lambda}(5100\ \text{Å})$ is the continuum luminosity at 5100 Å. The bolometric correction factor (k_{bol}) should also be adjusted for source inclination. For type 1 AGNs (typical inclination of ~56°), the correction factor is ~1.4, while for face-on accretion disks it is ~2.5 (Netzer 2019). Due to the lack of reliable inclination information, we adopted an average value of 2, as done by Crepaldi et al. (2025).

To determine L_{bol}, we first needed the continuum luminosity at 5100 Å. This parameter can be directly measured from the spectrum in non-jetted sources; however, in jetted AGNs, the jet contributes significantly to the continuum, making it difficult to disentangle from the thermal emission of the accretion disk. In such cases, line properties must instead be used. To this end, we applied the relation from Dalla Bontà et al. (2020), which connects $\lambda L_{\lambda}(5100\ \text{Å})$ to $L_{H\beta,\ broad}$:

$$\log\left[\lambda L_{\lambda}(5100\ \text{Å})\right] = (43.396 \pm 0.018) + (1.003 \pm 0.022)$$
$$\times \left[\log\left(\frac{L_{H\beta_{broad}}}{erg\ s^{-1}}\right) - 41.746\right]. \quad (7)$$

This approach relies entirely on the properties of the Hβ line.

For objects in which Hβ is undetected or affected by absorption, we used either the Mg II λ2800 or [O III]λ5007 lines. For the Mg II line, we used an analogous procedure to that applied for Hβ, calculating the expected continuum luminosity at 3000 Å, $\lambda L_\lambda(3000\,\text{Å})$, from the line properties. Combining Eqs. 8 and 7 from Trakhtenbrot & Netzer (2012), we obtain

$$\log\left[\frac{\lambda L_\lambda(3000\,\text{Å})}{10^{44}\,\text{erg s}^{-1}}\right] = 0.08 + 0.81 \times \log\left(\frac{L_{\text{Mg II}}}{10^{42}\,\text{erg s}^{-1}}\right), \qquad (8)$$

the result of which can be inserted in the corresponding relation for the Eddington ratio of Netzer (2019):

$$L_{\text{bol}} = k_{\text{bol}} \times \lambda L_\lambda(3000\,\text{Å}); \quad k_{\text{bol}} = 19 \cdot \left[\frac{\lambda L_\lambda(3000\,\text{Å})}{10^{42}\,\text{erg s}^{-1}}\right]^{-0.2}. \quad (9)$$

The adopted equation for the [O III] case, from Zhang & Feng (2017), is

$$\log\left[\frac{\lambda L_\lambda(5100\,\text{Å})}{\text{erg s}^{-1}}\right] = (17.28\pm0.98)\cdot\log\left(\frac{L_{\text{[O III]}_{\text{core}}}}{\text{erg s}^{-1}}\right)+(0.65\pm0.02), \quad (10)$$

where $L_{\text{[O III]}_{\text{core}}}$ is the luminosity of the core component of the [O III]λ5007 line. As for the black hole mass, Eddington ratios derived from the [O III]λ5007 line should be considered as upper limits. The results are summarized in Table A.1.

5. Notes on individual objects

In the following, we provide the emission lines fitting details for each source, along with the explanation for the new classification. The fitting parameters are reported in Table A.1, while the spectra are plotted in Fig. B.1.

5.1. J0102+4214

The GTC spectrum is significantly affected by noise. The Hβ–[O III] complex shows a prominent bump and is partially obscured by telluric absorption, which may result from Fe II emission or host-galaxy contamination. This prevents us from proposing a definitive classification of the AGN. To extract physical parameters, we fitted the Mg IIλ2800 line, as reported in Table A.1. A tentative fit of the Hβ line with a single Lorentzian profile yields FWHM(Hβ) = (2931 ± 980) km s^{-1}. This value is consistent with the estimate reported by Shaw et al. (2012), FWHM(Hβ) ~ 1900 km s^{-1}, but does not support a classification as NLS1. The [O III]$\lambda\lambda$4959, 5007 lines are severely affected by telluric absorption and buried in the noise. Consequently, we are unable to provide a revised classification for this object and therefore adopt the NLS1 classification reported by Foschini et al. (2022).

5.2. J0224+0700

The GTC spectrum reveals a few oxygen lines ([O II]λ3727 and [O III]$\lambda\lambda$4959,5007), as well as Mg IIλ2800 emission. In this case, telluric absorptions are prominent in both the Hβ and Hγ regions, preventing us from characterizing the line profiles or measuring their FWHM. On the other hand, the Mg II line is relatively unaffected by atmospheric absorption, allowing us to derive the black hole mass and the Eddington ratio. We report the same classification proposed by Foschini et al. (2022): NLS1.

5.3. J0422−0644

The UT1 spectrum shows multiple emission lines, both permitted (Hα, Hβ, and Hγ) and forbidden ([O III]$\lambda\lambda\lambda$4363, 4959, 5007). The Hβ–[O III] region is characterized by prominent Fe II emission, with R_{4570} ~ 1.19. After subtracting the Fe II contribution, we fitted the Hβ line using three Gaussian components (two broad and one narrow), and modeled the [O III] lines with single Gaussian profiles. The resulting total FWHM(Hβ) = (1940 ± 119) km s^{-1}, placing the object in the classical NLS1 family. Finally, the [O III]/Hβ flux ratio is approximately 0.22, confirming the relative faintness of the oxygen lines compared to the hydrogen lines. From these parameters we can propose a classification of NLS1.

5.4. J0442−0017

Luna-Cervantes et al. (2024) studied in detail the spectral energy distribution of this AGN and proposed a hybrid nature, between NLS1 and FSRQ. The UT1 spectrum is noisy and affected by atmospheric absorption features; however, the Hβ–[O III] region is only partially impacted. The Fe II emission contributes significantly, with R_{4570} ~ 1.05, although the He IIλ4686 line is also present in the same spectral region. The best fit for the Hβ line was obtained using a Lorentzian profile, while the [O III]$\lambda\lambda$4959,5007 lines were modeled with single Gaussians. The resulting total FWHM(Hβ) = (3518 ± 1218) km s^{-1}, outside the range typically associated with NLS1s, although the large uncertainty – mainly due to the noise level in the Hβ region – limits the robustness of this measurement. The [O III]/Hβ flux ratio is ~0.90, consistent with type 1 AGN properties. Given the large uncertainty on the FWHM(Hβ), our results are consistent with those of Shaw et al. (2012) and Foschini et al. (2022) while also being compatible with a BLS1 classification. Considering the central value of the Hβ width, we suggest a BLS1 classification, although higher-resolution spectra are required to confirm this result.

5.5. J0515−4556

The UT1 spectrum reveals all the main optical features, with a not negligible Fe II contribution (R_{4570} ~ 0.44). The [O III]$\lambda\lambda$4959,5007 lines display two peculiar characteristics: a blueshift of the entire feature by approximately 132 km s^{-1}, and a flux ratio of about 2, which deviates from the theoretical value of ~3 (as can be seen from Fig. B.1). This can be the result of a spurious spike under [O III]λ4959, or due to the very broad component found in Hβ. The Hβ line was modeled with three Gaussian components, and the resulting profile shows a redshifted very broad component (Δv ~ 3700 km s^{-1}). Furthermore, the [O III]/Hβ flux ratio is ~0.77. The asymmetric profile of Hβ can be the result of an NLS1 or and IS with a red wing. Given the γ-ray detection for this AGN, the orientation favor the type 1 classification for this object, but does not exclude the IS one. The total FWHM(Hβ) = (1534 ± 85) km s^{-1}. Due to these considerations, we propose a classification in between NLS1 and IS, to disentangle between the two, intermediate- or high-resolution spectra are needed.

5.6. J0521−1734

The UT1 spectrum shows a relatively noisy red part, but the Hβ–[O III] region is not affected by these fluctuations. The best fit for Hβ was obtained with a single Gaussian component,

with its FWHM tied to that of [O III], yielding FWHM([O III]) = $(845 \pm 30)\,\mathrm{km\,s^{-1}}$. The strength of the [O II]$\lambda3727$ line suggests a possible low-ionization nuclear emission-line region (LINER) nature for this AGN. However, a classification as a SY2 appears more likely, given the profiles of [O III]$\lambda5007$ and Hβ. In this scenario, J0521−1734 could be interpreted either as a misaligned AGN or as a true SY2 lacking a BLR (e.g., Marin et al. 2025). Distinguishing between the LINER and SY2 scenarios requires high- or intermediate-resolution spectroscopy with broader spectral coverage, ideally including Hα to enable the construction of diagnostic diagrams such as those developed by Baldwin et al. (1981) and Veilleux & Osterbrock (1987). Moreover, to confirm a possible absence of the BLR, polarized-light observations would be necessary.

5.7. J0932+5306

In the GTC spectrum, all the main optical features are clearly detected. The iron emission is negligible, which leave space to the detection of the He II$\lambda4686$ line. The best fit for the Hβ line was obtained using a combination of Gaussian components, yielding a total FWHM(Hβ) = $(1439 \pm 88)\,\mathrm{km\,s^{-1}}$. Each of the [O III] lines was modeled with a single Gaussian. The [O III]/Hβ flux ratio is ∼1.50, a value consistent with those typically observed in NLS1 galaxies. The relatively narrow Hβ line width and the weakness of the [O III] lines both support a classification as NLS1, despite the absence of significant Fe II emission. Similar cases of NLS1s with faint or undetectable Fe II features have been reported in the literature (e.g., Pogge 2011). We therefore confirm the classification of NLS1 proposed by Foschini et al. (2022).

5.8. J1048−1912

The UT1 spectrum shows fluctuations in the Hβ–[O III] region. We fitted oxygen lines with a single Gaussian each and a combination of two Gaussians for Hβ. The resulting Hβ profile is typical of an IS object, where the narrow and the broad components are clearly separable. The narrow component present a FWHM(Hβ) totally dominated by the instrumental broadening, as the one of [O III]$\lambda5007$. The Hβ broad component present a FWHM(Hβ) = $(6040 \pm 189)\,\mathrm{km\,s^{-1}}$ with a significant shift to the red with $\Delta v \sim 1528\,\mathrm{km\,s^{-1}}$. The global FWHM(H$\beta$) is consistent with the value reported by Murdoch et al. (1984). The iron contribution is negligible ($R_{4570} \sim 0$), and the [O III]/Hβ ratio is approximately 0.81. This allows us to reclassify the object as an IS, given the composite profile of Hβ. Following the classification scheme proposed by Whittle (1992), the IS type can be obtained calculating the ratio between the fluxes of $R_{Sy-type} = F(\text{[O III]})/F(\text{H}\beta)$. In this case we obtain a Seyfert 1.5 type.

5.9. J1102+5251

The GTC spectrum shows a negligible iron contribution ($R_{4570} \sim 0$) and a peculiar Hβ profile, composed of a narrow core and a prominent red wing. The FWHM of the [O III] lines and of the narrow component of Hβ are entirely dominated by instrumental broadening, whereas the broad component of Hβ has FWHM = $(3051 \pm 296)\,\mathrm{km\,s^{-1}}$ and is redshifted by $\Delta v \sim 590\,\mathrm{km\,s^{-1}}$. This line shape can be interpreted as consistent with an IS. The [O III]/Hβ flux ratio is ∼1.32, which is compatible with values observed in both classes. Based on these considerations – particularly the limitations imposed by instrumental

broadening – we propose this AGN be classified as an IS. Further observations with higher spectral resolution are required to confirm this scenario.

5.10. J1154+4037

The GTC spectrum is affected by several spurious peaks, which were subsequently removed. The final spectrum shows a prominent Mg II$\lambda2800$ line with FWHM = $(10098 \pm 297)\,\mathrm{km\,s^{-1}}$, while the H$\beta$–[O III] region is completely buried in the noise, preventing a definitive classification. Foschini et al. (2022) reported an NLS1 classification, but given the broadness of the Mg II$\lambda2800$ line, this does not appear reliable. As a consequence of the broad Mg II$\lambda2800$ line, the calculated black hole mass is the highest in the sample, with $\log(M_{\mathrm{BH}}/M_\odot) = (9.32 \pm 0.06)$. This result highlights the need for further investigation into the nature of the source, given that NLS1s are usually hosted in low-mass galaxies. We therefore propose classifying it as AMB.

5.11. J1202−0528

The UT1 spectrum displays all the main optical features, including both permitted and forbidden emission lines. The iron contribution is estimated to be $R_{4570} \sim 1.22$. The Hβ line was fitted with a combination of two Gaussian components, resulting in a total FWHM(Hβ) = $(1445 \pm 57)\,\mathrm{km\,s^{-1}}$, while the [O III]$\lambda\lambda4959,5007$ lines were modeled with two Gaussians each (core and outflow components). The [O III]/Hβ ratio is ∼0.83. These properties support the classification of this object as an NLS1.

5.12. J1246−2548

The Hβ line is fitted with two Gaussian components, resulting in a total FWHM(Hβ) = $(1430 \pm 266)\,\mathrm{km\,s^{-1}}$, which lies within the typical range for NLS1s. The broad component appears redshifted by $\Delta v \sim 420\,\mathrm{km\,s^{-1}}$. The [OIII]$\lambda\lambda4959,5007$ lines are prominent, but their FWHM is completely dominated by the instrumental broadening. The flux ratio [O III]/H$\beta \sim 0.41$ favor the classification of NLS1. The iron emission is negligible, with $R_{4570} \sim 0$, but the prominent telluric absorption in the blue part of the iron emission prevented us from properly fitting these lines. Overall, we propose a classification of NLS1.

5.13. J1310+5514

In the GTC spectrum, the Hβ–[O III] region appears very noisy due to its proximity to the grism efficiency drop[5], and is therefore considered as an artifact. For this reason, we excluded it from the final spectrum. The physical parameters were estimated from the Mg II$\lambda2800$ line, fitted with a Lorentzian profile, which yields FWHM = $(2271 \pm 38)\,\mathrm{km\,s^{-1}}$. New observations are required to establish a robust classification of this source. We therefore maintain the NLS1 classification proposed by Foschini et al. (2022).

5.14. J1331−1325

The UT1 spectrum displays all the main optical emission lines, from [O II]$\lambda3727$ to [S II]$\lambda\lambda6716,6731$. The iron contribution is

---

[5] https://www.gtc.iac.es/instruments/osiris/media/OSIRIS-R1000.jpg

negligible ($R_{4570} \sim 0$). Hβ presents a peculiar profile with a red bump ($\Delta v \sim 350 \, \mathrm{km \, s^{-1}}$), best fitted with three Gaussian profiles. The resulting total FWHM(Hβ) = $(575 \pm 94) \, \mathrm{km \, s^{-1}}$. The [O III]$\lambda\lambda$4959,5007 lines are fitted with a single Gaussian each, and the [O III]/Hβ ratio is $\sim$2.21. Considering the shape of the Hβ profile, we suggest an IS classification for this AGN.

5.15. J1818+0903

The UT1 spectrum displays all the main optical features, from [O II]λ3727 to [O III]λ5007. The iron emission yields $R_{4570} \sim 0.97$. The Hβ line was fitted using a Lorentzian component, resulting in a FWHM(Hβ) = $(1418 \pm 335) \, \mathrm{km \, s^{-1}}$. The [O III] lines were fitted with a single Gaussian, but their FWHM is dominated by the instrumental broadening. The [O III]/Hβ ratio is $\sim$0.98. Based on these results, we suggest this AGN be classified as an NLS1.

5.16. J1902−6748

The UT1 spectrum covers all the main optical features, including Hα. The iron contribution is present with $R_{4570} \sim 0.79$, and blended also with the He IIλ4686 line. The best fit for the Hβ line was obtained using a combination of three Gaussian components: the FWHM of the narrow component was tied to that of [O III], while the broad component is composed of two bumps, the broadest of which is redshifted by $\Delta v \sim 2400 \, \mathrm{km \, s^{-1}}$. A similarly asymmetric profile is also visible in the Hδ line. The total FWHM(Hβ) = $(1015 \pm 117) \, \mathrm{km \, s^{-1}}$. The [O III]/H$\beta$ flux ratio is $\sim$2.24. This case closely resembles the one discussed in Sect. 5.5. For this reason, we propose a classification that is intermediate between NLS1 and IS. Further investigations, including higher-resolution spectroscopy, are needed to distinguish between the two scenarios.

5.17. J2325−3559

The UT1 spectrum displays the typical features of an NLS1: faint [O III]$\lambda\lambda$4959,5007 lines with [O III]/Hβ $\sim$ 0.58, strong Fe II emission with $R_{4570} \sim 1.58$, and a global FWHM(Hβ) = $(971 \pm 75) \, \mathrm{km \, s^{-1}}$. The H$\beta$ line was fitted using a single Lorentzian profile, while the [O III] lines show a core component and prominent blue wings with $\Delta v \sim 770 \, \mathrm{km \, s^{-1}}$. Based on these properties, we classify the object as an NLS1.

5.18. J2354−0958

From the analysis of the UT1 optical spectrum, we conclude that the previous identification of [O II]λ3727 (Drinkwater et al. 2018) was incorrect. In the revised interpretation, we identify three lines: Mg IIλ2800, [O II]λ3727, and Hγ. Based on these features, we calculated a redshift of $z = (0.9920 \pm 0.0023)$, which is consistent with the value reported by Massaro et al. (2015). The spectrum is relatively noisy, and Hγ lies near the edge of the spectral range, limiting its usefulness for classification purposes. The Mg II line displays a broad profile, pointing toward the BLS1 nature. Due to the absence of significant Balmer lines, we do not propose a new classification for J2354−0958 and report the one proposed by Foschini et al. (2022): AMB.

6. Discussion

In this work we analyzed the optical spectra of 18 sources extracted from Foschini et al. (2022), which in turn are derived

from the 4FGL catalog compiled from observations by the *Fermi* satellite. The 4FGL catalog is predominantly populated by BL Lac objects, FSRQs, and unclassified sources. However, it also includes other types of AGNs, such as misaligned AGNs, NLS1s, Seyfert galaxies, and changing-look AGNs (CL-AGNs) (Foschini et al. 2022).

6.1. Classes of γ-ray-emitting AGNs

Our spectroscopic analysis confirms the presence of a variety of AGN types. Specifically, we identified two new NLS1s (J0422−0644 and J2325−3559), three ISs (J1048−1912, J1102+5252, and J1331−1325), two AMB cases showing characteristics between NLS1s and ISs (J0515−4556 and J1902−6748), one BLS1 (J0442−0017), and one SY2 (J0521−1734). In addition, we confirmed the classification of four previously known NLS1s. For the remaining five sources, a reliable classification was not possible due to poor data quality or limited spectral coverage – as in the case of J2354−0958, where the available spectrum was insufficient for a robust analysis. Among these, J1154+4037 was reported as AMB because the measured width of the Mg IIλ2800 line is no longer compatible with the NLS1 class; however, a new solid classification is still not possible.

When combined with the results of Foschini et al. (2022), our findings confirm that different classes of AGNs are capable of producing powerful jets detectable in γ-rays. The separation into classes of jetted AGNs, based on the Foschini et al. (2022) sample together with three additional objects from Paliya et al. (2024) and Li et al. (2023), some of which are reclassified according to the analysis presented in this paper, is illustrated in Fig. 1. From this plot, it is clear that the majority (about 40%) are BL Lacs, where the jet dominates the observed spectrum. Another large fraction (about 23%) consists of FSRQs, γ-ray sources characterized by strong optical lines and Balmer lines with FWHM > 2000 $\mathrm{km \, s^{-1}}$. A further $\sim$29% of the sample remains unclassified.

Beyond these three dominant groups, several minority classes are also represented. The most numerous are misaligned AGNs, which include radio galaxies, soft-spectrum radio quasars, and compact steep-spectrum quasars. Their classification, based on radio properties and inherited from 4FGL and Foschini et al. (2022), remains unchanged in this work.

Other small fractions include AMB objects (1.4%), Seyferts (1.2%), NLS1s (1.1%), and CL-AGNs (1.1%). The presence of γ-NLS1s remains of particular interest, as it challenges the standard blazar sequence scenario. Their number is steadily increasing, as confirmed by this study. Seyfert-type sources, on the other hand, comprise Seyfert 1s (SY1s), SY2s, ISs, and LINERs. While Sy1 objects are compatible with the observed γ-ray emission, SY2 (e.g., J0521−1734) and IS (e.g., J1048−1912, J1102+5251, and J1331−1325) imply an orientation inconsistent with the jet properties. This misalignment could be due to different mechanisms, such as a recent merger (Olguín-Iglesias et al. 2020), jet instabilities causing a twist (Lalakos et al. 2024), or obscuration by interstellar dust in the host galaxy. In the dust case, the AGN may be misaligned with the galaxy disk (e.g., Schmitt et al. 2002; Hopkins et al. 2012), producing a partial covering of the BLR, this misalignment is usually a consequence of a recent merger. Alternatively, dust could have been redistributed by jet-ISM interaction, introducing line-of-sight obscuration. A variable line-of-sight obscuration could also explain the CL-AGN phenomena (see Ricci & Trakhtenbrot 2023 for a recent review). Finally, in J0521−1734, a true SY2 scenario
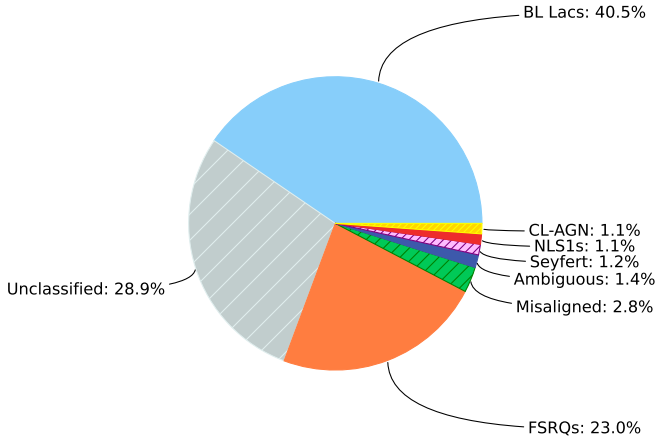
Fig. 1. Distribution of different source classes in the 4FGL catalog. Percentages indicate the updated number of objects in each class, based on Foschini et al. (2022) and revised according to the analysis presented in this work and other recent studies. Specifically, 2980 sources are from Foschini et al. (2022), 2 (J0105+1912 and J0933−0013) are from Paliya et al. (2024), and 1 (J0959+4600) is from Li et al. (2023).

cannot be excluded. In this case, the BLR is intrinsically absent, so that the AGN is observed face-on but does not display broad permitted lines.

6.2. Physical parameters

The physical parameters derived for our sample span a wide range. The black hole masses, derived by relations that take the jet contribution to the continuum optical emission into account, lie between $\log(M_{\mathrm{BH}}/M_\odot) = (6.25 \pm 0.40)$ and (9.32 ± 0.06), with upper limits reaching up to $\log(M_{\mathrm{BH}}/M_\odot) = 10.23$. The Eddington ratios, instead, range from $R_{\mathrm{Edd}} = (2.07 \pm 0.16)$ to (0.05 ± 0.03).

As expected, both the newly identified and the confirmed NLS1s exhibit black hole masses on the lower end of the AGN spectrum – typically within the range $10^{6-8}\ M_\odot$, compared to $10^{8-9}\ M_\odot$ for other jetted AGNs. In our sample, the NLS1s show a mean value of $\log(M_{\mathrm{BH}}/M_\odot) = (7.36 \pm 0.68)$. If we include the AMB objects with properties between NLS1s and ISs, the mean becomes $\log(M_{\mathrm{BH}}/M_\odot) = (7.33 \pm 0.62)$, which still falls within the typical NLS1 mass range.

The ISs also exhibit black hole masses within this range. However, it is important to note that in the ISs case the classical virial mass estimates are affected by partial obscuration of the BLR. Since the black hole mass is computed from the broad component of the Hβ emission line flux (see the $L_{\mathrm{H}\beta_{\mathrm{broad}}}$ term in Eq. 4), any attenuation of this component can lead to an underestimation. Therefore, for these sources, the derived black hole mass should be considered a lower limit to the actual value.

The Eddington ratio was calculated by accounting for the possible contribution of the relativistic jet to the optical continuum, particularly when using Hβ- and Mg IIλ2800-based estimates. The highest R_{Edd} in our sample are observed in J0224+0700 and J2325−3559, as expected for NLS1s. NLS1s are typically associated with slim accretion disks, which are thought to be sustained by high, or even super-Eddington, accretion rates (Shakura & Sunyaev 1973; Abramowicz et al. 1980, 1988; Balbus & Hawley 1991; Wang et al. 1999; Mineshige et al. 2000; Sądowski et al. 2014).
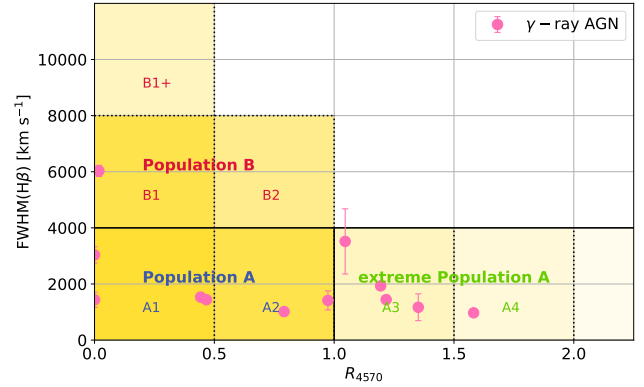
Fig. 2. FWHM(Hβ_{broad})–R_{4570} plane that defines the quasar MS. Pop. A and B are shown, together with their finer subdivisions. Shaded regions indicate the areas populated by quasars, with the color intensity representing the source density in each region. The pink points represent the objects in the current sample for which the FWHM(Hβ_{broad}) and R_{4570} were measured.

These regimes are often interpreted as indicative of rapidly growing black holes in AGNs at an early evolutionary stage.

6.3. The role of the R_{4570} index

A key diagnostic parameter in our analysis is the R_{4570} index, which quantifies the strength of the optical Fe II emission relative to the Hβ line. This parameter plays a fundamental role in the classification of AGNs along the so-called quasar main sequence (MS). The MS represents the distribution of type 1 quasars in the FWHM(Hβ_{broad})–R_{4570} plane, and is widely used to investigate the diversity of quasar spectral properties. Within this plane (see the example in Fig. 2), a grid of spectral types has been defined: types A1 through A4 correspond to increasing Fe II emission, whereas B1, B1+, and B1++ indicate increasing FWHM of the broad Hβ component. A horizontal threshold at FWHM(Hβ_{broad}) $\sim 4000\ \mathrm{km\,s^{-1}}$ separates Population A (pop. A) from Population B (pop. B). These populations are believed to group sources sharing broadly similar physical conditions and BLR geometry.

Boroson & Green (1992) identified several physical drivers that can influence the position of a quasar within the MS, including: R_{Edd}, M_{BH}, the BLR cloud covering factor, the anisotropy of the continuum emission, the viewing angle of the source with respect to the observer, the velocity distribution of BLR clouds, and the ionization parameter. These factors contribute to shaping both the line widths and the strength of Fe II emission observed in quasar spectra, and hence their location along the MS. The R_{4570} index therefore serves not only as a classification tool, but also as a tracer of the physical conditions in the nuclear region of AGNs (Marziani et al. 2018).

In this framework, NLS1s occupy the lower-right region of the MS diagram, due to their relatively narrow Hβ lines and typically strong Fe II emission. In other words, NLS1s belong to pop. A, or even to the so-called extreme pop. A (defined as sources with $R_{4570} > 1$). As described by Marziani et al. (2018), the differences between pop. A and B extend beyond line widths: pop. A sources typically show symmetric, often Lorentzian-shaped Balmer profiles, while pop. B sources exhibit broader, multicomponent profiles with possible redward asymmetries. Additionally, lines such as C IVλ1549, Mg IIλ2800, and

the [O III]$\lambda\lambda$4959,5007 doublet often show significant blueshifts in pop. A sources. Other trends include a higher probability of radio-loudness and a flatter soft X-ray slope among pop. B objects (Grupe 2004; Zamfir et al. 2010).

Within our sample, all sources classified as NLS1 exhibit symmetric Hβ profiles, fitted with either a single Lorentzian or multiple Gaussians. Asymmetric Balmer lines, instead, are found in sources classified as IS or in the AMB cases between NLS1 and IS. All NLS1s in our sample belong to pop. A, as expected by construction. The AMB cases also fall within pop. A. One exception is the source J1048−1912, which displays a very broad H$\beta_{\rm broad}$ line (FWHM $\sim$ 6101 km s^{-1}) and lacks detectable Fe II emission; it is therefore assigned to pop. B. These considerations strength our classification, within the MS framework.

7. Conclusions

We have increased the number of optically and spectroscopically confirmed NLS1s with γ-ray emission to 26. This number increases further to 36 – the 34 listed in Table C.1 and the 2 additional borderline NLS1–IS objects reported in this work – if we include AMB cases. The complete list of γ-ray-emitting NLS1s is provided in Table C.1.

To resolve the ambiguous classification and to provide a more robust characterization of those sources for which we currently report only the classifications from Foschini et al. (2022), higher-spectral-resolution datasets (e.g., as obtained by VLT/X-shooter) are necessary. The X-shooter spectra could allow us to perform a detailed optical analysis of the selected sources, enabling accurate measurements of line profiles and physical parameters. They could also facilitate the identification of peculiar cases, similar to the one recently reported by Dalla Barba et al. (2025), and ultimately improve our understanding of the diversity among γ-ray-emitting AGNs.

References

Abramowicz, M. A., Calvani, M., & Nobili, L. 1980, ApJ, 242, 772
Abramowicz, M. A., Czerny, B., Lasota, J. P., & Szuszkiewicz, E. 1988, ApJ, 332, 646
Antonucci, R. 1993, ARA&A, 31, 473
Balbus, S. A., & Hawley, J. F. 1991, ApJ, 376, 214
Baldwin, J. A., Phillips, M. M., & Terlevich, R. 1981, PASP, 93, 5
Berton, M., Caccianiga, A., Foschini, L., et al. 2016, A&A, 591, A98
Berton, M., Björklund, I., Lähteenmäki, A., et al. 2020, Contrib. Astron. Obs. Skalnate Pleso, 50, 270
Berton, M., Peluso, G., Marziani, P., et al. 2021, A&A, 654, A125
Bianchi, S., Panessa, F., Barcons, X., et al. 2012, MNRAS, 426, 3225
Blandford, R., Meier, D., & Readhead, A. 2019, ARA&A, 57, 467
Boroson, T. A., & Green, R. F. 1992, ApJS, 80, 109
Chen, K., Halpern, J. P., & Filippenko, A. V. 1989, ApJ, 339, 742
Collin, S., Kawaguchi, T., Peterson, B. M., & Vestergaard, M. 2006, A&A, 456, 75

Cracco, V., Ciroi, S., Berton, M., et al. 2016, MNRAS, 462, 1256
Crepaldi, L., Berton, M., Dalla Barba, B., et al. 2025, A&A, 696, A74
Dalla Barba, B., Berton, M., Foschini, L., et al. 2023, Physics, 5, 1061
Dalla Barba, B., Berton, M., Foschini, L., et al. 2025, A&A, 698, A320
Dalla Bontà, E., Peterson, B. M., Bentz, M. C., et al. 2020, ApJ, 903, 112
Dimitrijević, M. S., Kovačević, J., Popović, L., Dačić, M., & Ilić, D. 2007, in Fifty Years of Romanian Astrophysics, eds. C. Dumitrache, N. A. Popescu, M. D. Suran, & V. Mioc (AIP), AIP Conf. Ser., 895, 313
Drinkwater, M. J., Byrne, Z. J., Blake, C., et al. 2018, MNRAS, 474, 4151
Dumont, A. M., & Collin-Souffrin, S. 1990, A&A, 229, 313
Foschini, L. 2017, Front. Astronomy and Space Sciences, 4, 6
Foschini, L., Ciroi, S., Berton, M., et al. 2019, Universe, 5, 199
Foschini, L., Lister, M. L., Andernach, H., et al. 2022, Universe, 8, 587
Gaskell, C. M. 1996, ApJ, 464, L107
Ghisellini, G., Tavecchio, F., Maraschi, L., Celotti, A., & Sbarrato, T. 2014, Nature, 515, 376
Goad, M. R., Korista, K. T., & Ruff, A. J. 2012, MNRAS, 426, 3086
Goodrich, R. W. 1989, ApJ, 342, 224
Greene, J. E., & Ho, L. C. 2005, ApJ, 627, 721
Grupe, D. 2004, AJ, 127, 1799
Ho, L. C., & Kim, M. 2014, ApJ, 789, 17
Hopkins, P. F., Hayward, C. C., Narayanan, D., & Hernquist, L. 2012, MNRAS, 420, 320
Järvelä, E., Berton, M., Ciroi, S., et al. 2020, A&A, 636, L12
Kaspi, S., Smith, P. S., Netzer, H., et al. 2000, ApJ, 533, 631
Keel, W. C. 1980, AJ, 85, 198
Kollatschny, W., & Zetzl, M. 2011, Nature, 470, 366
Kovačević, J., Popović, L. Č., & Dimitrijević, M. S. 2010, Mem. Soc. Astron. It. Suppl., 15, 176
Lalakos, A., Tchekhovskoy, A., Bromberg, O., et al. 2024, ApJ, 964, 79
Li, Y.-J., Liao, N.-H., Sheng, Z.-F., et al. 2023, A&A, 676, A9
Luna-Cervantes, J., Tramacere, A., & Benítez, E. 2024, MNRAS, 532, 3729
Marin, F., Hutsemékers, D., Jiang, C. Z., et al. 2025, A&A, 695, A55
Marscher, A. P., Jorstad, S. G., D'Arcangelo, F. D., et al. 2008, Nature, 452, 966
Marziani, P., Dultzin, D., Sulentic, J. W., et al. 2018, Front. Astron. Space Sci., 5, 6
Massaro, E., Maselli, A., Leto, C., et al. 2015, Ap&SS, 357, 75
Mineshige, S., Kawaguchi, T., Takeuchi, M., & Hayashida, K. 2000, PASJ, 52, 499
Miniutti, G., Saxton, R. D., Rodríguez-Pascual, P. M., et al. 2013, MNRAS, 433, 1764
Murdoch, H. S., Hunstead, R. W., & White, G. L. 1984, PASA, 5, 341
Netzer, H. 2019, MNRAS, 488, 5185
Olguín-Iglesias, A., Kotilainen, J., & Chavushyan, V. 2020, MNRAS, 492, 1450
Osterbrock, D. E., & Koski, A. T. 1976, MNRAS, 176, 61P
Osterbrock, D. E., & Pogge, R. W. 1985, ApJ, 297, 166
Padovani, P., Alexander, D. M., Assef, R. J., et al. 2017, A&ARv, 25, 2
Paliya, V. S., Stalin, C. S., Domínguez, A., & Saikia, D. J. 2024, MNRAS, 527, 7055
Pogge, R. 2003, Are there any true Seyfert 2 nuclei?, Chandra Proposal ID 05700639
Pogge, R. W. 2011, in Narrow-Line Seyfert 1 Galaxies and their Place in the Universe, eds. L. Foschini, M. Colpi, L. Gallo, et al., 2
Ricci, C., & Trakhtenbrot, B. 2023, Nat. Astron., 7, 1282
Riess, A. G., Yuan, W., Macri, L. M., et al. 2022, ApJ, 934, L7
Sądowski, A., Narayan, R., McKinney, J. C., & Tchekhovskoy, A. 2014, MNRAS, 439, 503
Schmitt, H. R., Pringle, J. E., Clarke, C. J., & Kinney, A. L. 2002, ApJ, 575, 150
Shakura, N. I., & Sunyaev, R. A. 1973, A&A, 24, 337
Shapovalova, A. I., Popović, L. Č., Burenkov, A. N., et al. 2012, ApJS, 202, 10
Shaw, M. S., Romani, R. W., Cotter, G., et al. 2012, ApJ, 748, 49
Sulentic, J. W., Marziani, P., Zamanov, R., et al. 2002, ApJ, 566, L71
Sulentic, J. W., Marziani, P., & Zamfir, S. 2009, New Astron. Rev., 53, 198
Tody, D. 1986, in Instrumentation in astronomy VI, ed. D. L. Crawford, SPIE Conf. Ser., 627, 733
Tody, D. 1993, in Astronomical Data Analysis Software and Systems II, eds. R. J. Hanisch, R. J. V. Brissenden, & J. Barnes, ASP Conf. Ser., 52, 173
Trakhtenbrot, B., & Netzer, H. 2012, MNRAS, 427, 3081
Urry, C. M., & Padovani, P. 1995, PASP, 107, 803
Veilleux, S., & Osterbrock, D. E. 1987, ApJS, 63, 295
Wang, J.-M., Szuszkiewicz, E., Lu, F.-J., & Zhou, Y.-Y. 1999, ApJ, 522, 839
Whittle, M. 1992, ApJS, 79, 49
Zamfir, S., Sulentic, J. W., Marziani, P., & Dultzin, D. 2010, MNRAS, 403, 1759
Zhang, X.-G., & Feng, L.-L. 2017, MNRAS, 468, 620

Appendix A: Fitting parameters and classification

Table A.1. Fitting parameters with the corresponding uncertainties, classifications, physical parameters, and measured redshift.

Name		Hβ			[O III]λ5007		Class. F22	New class.	$\log(M_{BH}/M_\odot)$	R_{Edd}	Methods	z_m
	Type	Flux [10^{-17} erg s^{-1}]	FWHM [km s^{-1}]	Type	Flux [10^{-17} erg s^{-1}]	FWHM [km s^{-1}]						
J0422−0644	G_n	43 ± 6	572*	G_c	58 ± 3	572 ± 36	FSRQ	**NLS1**	7.05 ± 0.53	0.13 ± 0.07	(A,D)	0.2417 ± 0.0007
	G_b	224 ± 46	2265 ± 385	-	-	-						
J0442−0017	L	120 ± 14	3518 ± 1218	G_c	81 ± 5	@	NLS1	**BLS1**	7.60 ± 0.43	0.23 ± 0.10	(A,D)	0.8467 ± 0.0016
J0515−4556	G_n	24 ± 2	192*	G_c	116 ± 1	192 ± 6	AMB	**NLS1/IS**	7.09 ± 0.66	0.05 ± 0.03	(A,D)	0.1946 ± 0.0004
	G_b	126 ± 5	1807 ± 291	-	-	-						
J0521−1734	G_n	14 ± 1	845*	G_c	43 ± 1	845 ± 30	FSRQ	**SY2**	<10.23	<0.01	(B,E)	0.3472 ± 0.0002
J0932+5306	G_n	36 ± 4	267*	G_c	316 ± 2	267 ± 5	NLS1	**NLS1**	7.74 ± 0.50	0.11 ± 0.06	(A,D)	0.5967 ± 0.0002
	G_b	174 ± 10	1813 ± 359	-	-	-						
J1048−1912	G_n	19 ± 1	@*	G_c	115 ± 1	@	NLS1	**IS**	8.01 ± 0.94	<0.09	(A,D)	0.5953 ± 0.0002
	G_b	124 ± 3	6040 ± 189	-	-	-						
J1102+5251	G_n	28 ± 3	@*	G_c	143 ± 2	@	NLS1	**IS**	7.38 ± 1.61	<0.49	(A,D)	0.6899 ± 0.0009
	G_b	80 ± 5	3043 ± 293	-	-	-						
J1202−0528	G_n	174 ± 18	@*	G_c	791 ± 23	@	NLS1	**NLS1**	7.86 ± 0.39	0.14 ± 0.06	(A,D)	0.3805 ± 0.0002
	G_b	954 ± 80	1843 ± 401	G_o	498 ± 24	1069 ± 45						
J1246−2548	G_n	86 ± 7	@*	G_c	247 ± 5	@	NLS1	**NLS1**	8.22 ± 0.88	0.10 ± 0.09	(A,D)	0.6372 ± 0.0002
	G_b	518 ± 14	4779 ± 149	-	-	-						
J1331−1325	G_n	15 ± 2	@*	G_c	84 ± 1	@	FSRQ	**IS**	6.48 ± 1.55	<0.20	(A,D)	0.2514 ± 0.0002
	G_b	23 ± 3	1175 ± 485	-	-	-						
J1818+0903	L	91 ± 8	1418 ± 335	G_c	120 ± 3	@	NLS1	**NLS1**	6.25 ± 0.40	0.79 ± 0.32	(A,D)	0.3542 ± 0.0004
J1902−6748	G_n	55 ± 3	@*	G_c	432 ± 2	@	FSRQ	**NLS1/IS**	7.21 ± 0.78	< 0.11	(A,D)	0.2542 ± 0.0002
	G_b	137 ± 11	1850 ± 799	-	-	-						
J2325−3559	L	212 ± 3	971 ± 75	G_c	125 ± 7	@	AMB	**NLS1**	6.32 ± 0.37	1.36 ± 0.51	(A,D)	0.3666 ± 0.0004
	-	-	-	G_o	70 ± 13	1424 ± 963						

Name		Mg II λ2800			[O II]λ3727		Class. F22	New class.	$\log(M_{BH}/M_\odot)$	R_{Edd}	Methods	z_m
	Type	Flux [10^{-17} erg s^{-1}]	FWHM [km s^{-1}]	Type	Flux [10^{-17} erg s^{-1}]	FWHM [km s^{-1}]						
J0102+4214	L	65 ± 1	2771 ± 82	-	-	-	NLS1	NLS1	7.89 ± 0.06	0.74 ± 0.01	(C,F)	0.8773 ± 0.0005
J0224+0700	L	86 ± 9	1408 ± 229	G_c	41 ± 4	@	NLS1	NLS1	7.08 ± 0.34	2.07 ± 0.16	(C,F)	0.5119 ± 0.0007
J1154+4037	L	223 ± 3	10098 ± 297	G_c	4 ± 1	<454	NLS1	**AMB**	9.32 ± 0.06	0.08 ± 0.01	(C,F)	0.9251 ± 0.0004
J1310+5514	L	97 ± 1	2271 ± 38	-	-	-	NLS1	NLS1	7.84 ± 0.04	1.28 ± 0.01	(C,F)	0.9251 ± 0.0004
J2354−0958	L	42.5 ± 0.9	4540 ± 158	G_c	6.0 ± 0.3	541 ± 56	AMB	**AMB**	7.62 ± 0.07	0.10 ± 0.01	(C,F)	0.9884 ± 0.0005
	-	-	-	G_o	70 ± 13	-						

Notes. Columns: name of the object, type of curve used to fit the components of the line (Lorentzian - L, narrow Gaussian - G_n, broad Gaussian - G_b, core Gaussian - G_c, and outflow Gaussian - G_o), flux, FWHM of the line along with the uncertainty, old classification from Foschini et al. (2022) (F22), the new proposed classification, M_{BH}, R_{Edd}, the used methods, and measured redshift. The FWHM values marked with * correspond to those associated with the narrow lines, while values marked with @ correspond to FWHM totally dominated by the instrumental contribution. The table is divided horizontally into two sections: the Hβ–[O III]λ5007 section and the Mg IIλ2800–[O II]λ3727 section. The classifications highlighted in bold correspond to cases in which the new spectra were useful either to confirm the classification proposed by Foschini et al. (2022) or to propose a new one. Methods: (A) for Dalla Bontà et al. (2020), (B) for Ho & Kim (2014), and (C) for Trakhtenbrot & Netzer (2012). The same is valid for the Eddington ratio, due its dependence on M_{BH}. In this case the methods are: (D) for the classical derivation of R_{Edd} from [O III]λ5007, (E) for the classical derivation of R_{Edd} from Hβ, and (F) for the derivation of R_{Edd} from Mg IIλ2800.
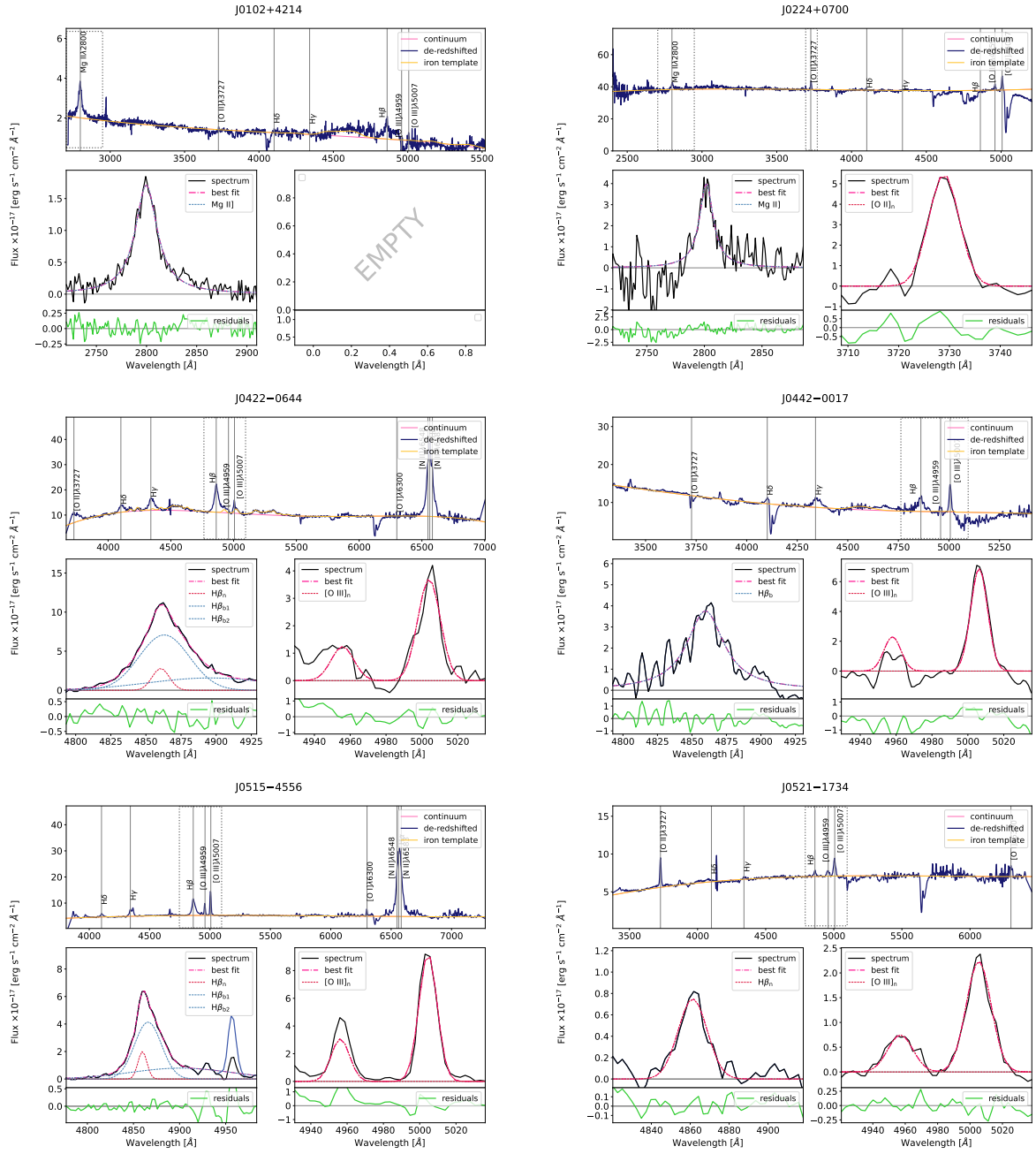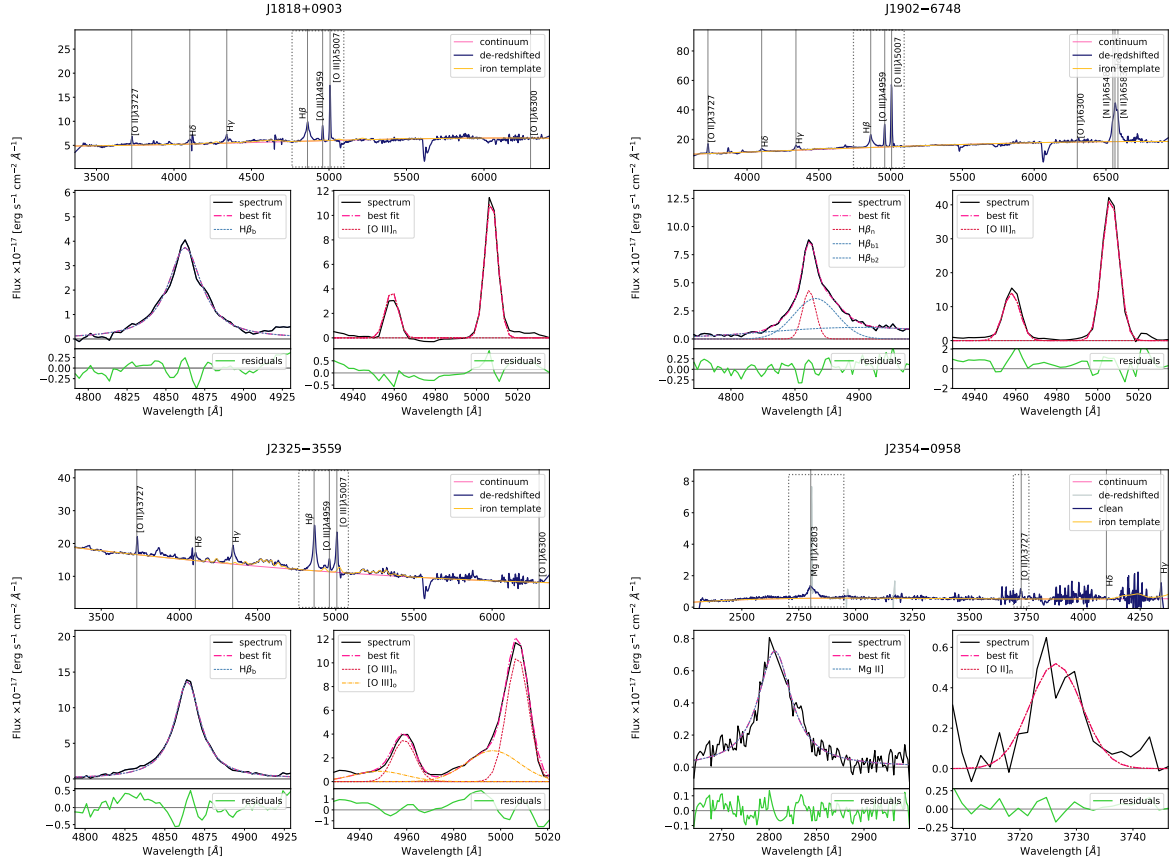
Appendix B: Plots

Fig. B.1. Spectra of the considered sources. Top panels: Redshift-corrected spectra with continuum and iron line fits overlaid. Dotted gray rectangles indicate the regions that are magnified in the lower panels, where detailed line fitting is performed. Bottom panels: Fitted emission lines (e.g., Hβ–[O III]λλ4959,5007 or Mg IIλ2800–[O II]λ3727), along with the corresponding residuals. Continued on the next page.

Appendix C: Optically confirmed γ-ray detected NLS1s

Table C.1. γ-NLS1s with the corresponding coordinates and the most recent reference for the classification.

Name	Alias	RA (J2000) [h:m:s]	Dec (J2000) [°:':"]	z	Classification reference
J0001+2113	TXS 2358+209	00:01:32.4	+21:13:36.3	0.438	a
J0010+2043	TXS 0007+205	00:10:28.7	+20:47:49.8	0.597	a
J0014−0500	WISE J001420.42−045928.7	00:14:20.4	−04:59:28.8	0.790	a
J0038−0204†	3C 17	00:38:20.5	−02:07:40.5	0.220	a
J0102+4214	GB6 J0102+4214	01:02:27.1	+42:14:18.9	0.877	b
J0105+1912†	TXS 0103+189	01:05:55.2	+19:12:28.0	0.879	a
J0224+0700	PKS 0221+067	02:24:28.4	+06:59:23.3	0.512	b
J0324+3412	1H 0323+342	03:24:41.2	+34:10:45.9	0.063	b
J0422−0644	PMN J0422−0643	04:22:10.8	−06:43:45.3	0.242	c
J0850+5108	SBS 0846+513	08:49:58.0	+51:08:29.0	0.584	a
J0932+5306	S4 0929+53	09:32:41.2	+53:06:33.8	0.597	c
J0933−0013†	PMN J0933−0012	09:33:23.0	−00:10:51.6	0.796	a
J0948+0022	PMN J0948+0022	09:48:57.3	+00:22:25.6	0.585	d
J0949+1749†	TXS 0946+181	09:49:39.8	+17:52:49.4	0.692	a
J0958+3222	3C 232	09:58:20.9	+32:24:02.2	0.530	a
J0959+4600	SDSS J095909.51+460014.3	09:59:09.5	+46:00:14.3	0.399	e
J1127+3618†	MG2 J112758+3620	11:27:58.9	+36:20:28.4	0.884	a
J1202−0528	PKS 1200−051	12:02:34.2	−05:28:02.5	0.381	c
J1208+5441	TXS 1206+549	12:08:54.3	+54:41:58.2	1.34	b
J1214−1926	PKS B1211−190	12:14:03.4	−19:21:42.8	0.149	b
J1246−2548	PKS 1244−255	12:46:46.8	−25:47:49.3	0.637	c
J1305+5118	IERS B1303+515	13:05:22.8	+51:16:40.3	0.787	a
J1310+5514	TXS 1308+554	13:11:03.2	+55:13:54.3	0.926	b
J1443+4728	B3 1441+476	14:43:18.6	+47:25:56.7	0.703	a
J1505+0326	PKS 1502+036	15:05:06.5	+03:26:30.8	0.407	a
J1520+4209†	B3 1518+423	15:20:39.7	+42:11:11.5	0.485	a
J1639+4129	MG4 J163918+4127	16:39:15.8	+41:28:33.7	0.690	a
J1644+2620	MG2 J164443+2618	16:44:42.5	+26:19:13.3	0.144	a
J1700+6830	TXS 1700+685	17:00:09.3	+68:30:07.0	0.301	b
J1818+0903	NVSS J181840+090346	18:18:40.1	+09:03:46.2	0.354	c
J1848+3217	B2 1846+32A	18:48:22.1	+32:19:02.6	0.798	b
J2118+0019†	PMN J2118+0013	21:18:17.4	+00:13:16.8	0.463	a
J2118−0723†	TXS 2116−077	21:18:53.0	−07:32:27.6	0.260	a
J2325−3559	CTS 0490	23:25:28.6	−35:57:54.2	0.367	c

Notes. References: (a) Paliya et al. (2024), (b) Foschini et al. (2022), (c) this work, (d) Dalla Barba et al. (2025), and (e) Li et al. (2023). Objects marked with † were originally classified as γ-NLS1s by Paliya et al. (2024), but after visual inspection of the SDSS spectra we suggest their reclassification as AMB, due to spectral features or poor data quality. Additional support for this ambiguity comes from the case of J2118−0723, which was reclassified from NLS1 to IS by Järvelä et al. (2020) after a detailed analysis.